Impact of Wall Slip on Screen Printing of Front-Side Silver Pastes for Silicon Solar Cells

Chenhui Xu, Markus Fieß, and Norbert Willenbacher

***Abstract*—Printing of narrow electrodes with higher aspect ratio challenges the formulation of silver paste for front-side metallization of silicon solar cells. Here, we have investigated four pastes differing in solvent composition. The onset of slip, slip velocity on steel and on emulsion over mesh (EOM) have been determined using rotational rheometry. In both cases, v increases linearly with applied stress τ. Its absolute value, the slope v/τ, and the slip layer thickness δ_{slip} vary in a wide range, depending on paste composition. Silver deposit, residual silver on the screen, the geometry of the printed electrodes, and the connections between busbar and fingers have been examined using gravimetric methods and optical microscopy. The silver deposit systematically increases, and accordingly, the residual silver on the screen decreases with increasing slip velocity. The busbar/fingers connection area narrows, whereas height and cross-sectional area of the electrodes increase with slip velocity. However, electrode width seems to be related to the pastes' yield stress. Mass deposit, shape of the busbar/finger connection, and electrode geometry are supposed to have an important impact on cell parameters, e.g., short-circuit current and fill factor. Accordingly, our results suggest that the slip behavior of the paste affects the overall cell efficiency.**

***Index Terms*—Screen printing, silicon solar cell, silver paste, wall slip.**

I. Introduction

SCREEN printing dominates the application of silver electrodes on the front side of silicon solar cells. Narrower electrodes reduce the shaded area, resulting in higher efficiency and lower silver consumption. However, this usually leads to smaller cross-sectional area, resulting in higher series resistance and lower efficiency. Thus, the aspect ratio should be increased. Typically, front-side silver pastes contain silver particles, glass frit, and the organic vehicle, which includes solvents, binders, and other additives [1], [2]. The vehicle transforms silver and glass powders into a printable paste. Essentially, all organic components are evaporated and burned during drying and firing. Processing behavior, printability, and printed electrodes' shape are tightly related to the flow properties of the pastes.

Manuscript received July 14, 2016; revised August 31, 2016 and October 20, 2016; accepted October 25, 2016. Date of publication November 24, 2016; date of current version December 20, 2016.

C. Xu is with the Group Applied Mechanics (AME), Institute for Mechanical Process Engineering and Mechanics, Karlsruhe Institute of Technology, 76128 Karlsruhe, Germany, and also with BASF SE, 67063 Ludwigshafen, Germany (e-mail: chenhui.xu@student.kit.edu).

M. Fieß is with BASF SE, 67063 Ludwigshafen, Germany (e-mail: markus.fiess@basf.com).

N. Willenbacher is with the Group Applied Mechanics (AME), Institute for Mechanical Process Engineering and Mechanics, Karlsruhe Institute of Technology, 76128 Karlsruhe, Germany (e-mail: norbert.willenbacher@kit.edu).

Color versions of one or more of the figures in this paper are available online at http://ieeexplore.ieee.org.

Digital Object Identifier 10.1109/JPHOTOV.2016.2626147

TABLE I
Formulation of Four Vehicles

	V1	V2	V3	V4
PSMA solution [wt%]	41.84	41.84	41.84	41.84
Thixatrol ST [wt%]	5.10	5.10	5.10	5.10
Disper Byk 111 [wt%]	2.04	2.04	2.04	2.04
Texanol [wt%]	51.02	46.94	43.88	40.82
Triacetin [wt%]	0.00	4.08	7.14	10.20

Previous rheological characterization of silver pastes usually focused on the evaluation of rheological parameters and phenomena such as yield stress, viscosity, and thixotropy [3]–[5]. Rheological evaluation usually relies on the assumption that the fluid adheres to the walls of the rheometer. However, highly concentrated suspensions show wall slip [6]. Due to the formation of a thin liquid layer at the gap boundary, the apparent viscosity is lower than the bulk viscosity [7]–[9]. Wall slip complicates the interpretation of the results of rheological measurements, since it is difficult to discern its influence on the distribution of shear stress and deformation in the gap. Yoshimura and Prud'homme developed a simplified model to determine slip velocity, shear rate, and true viscosity from measurements using plate–plate geometry with varying gap sizes [10]. A method to minimize slip effect is to increase the roughness of the rheometer walls or to use large gaps [11], [12].

However, it was found that wall slip can offer benefits during printing of paste. In stencil printing of solder pastes, wall slip enabled a reduction of printing defects [13], [14]. It was demonstrated that the formation of a slip layer reduced the adhesion of the paste on the stencil surface. This slip layer improved the paste release from the stencil aperture. However, to the best of our knowledge, the influence of wall slip on screen printing has not been investigated. In this study, we have investigated four silver pastes with different vehicles. Onset of slip and slip velocity were obtained from standard rotational rheometer experiments. All pastes were screen printed, and the dimensions of the printed electrodes were measured.

II. Paste Preparation

This study focused on the relation between slip, mass of deposited paste, and the dimensions of printed electrodes. Four pastes were prepared with identical silver content of 90.20 wt%, marked as P1–P4, but four kinds of organic vehicles marked as V1–V4, as shown in Table I. The average diameter of the silver particle is $D_{50} \sim 2$ μm according to certificate of analysis provided by supplier. The vehicles include a 25-wt% solution of

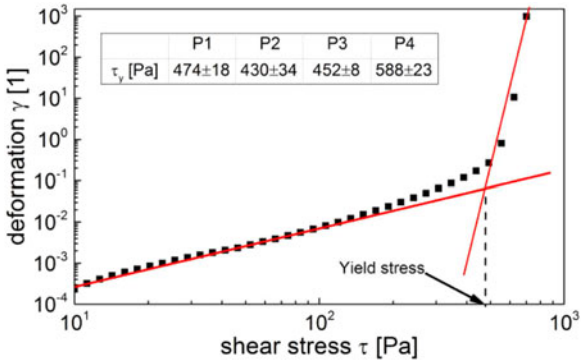

Fig. 1. Intersected point method to determine the yield stress and the yield stresses for four pastes.

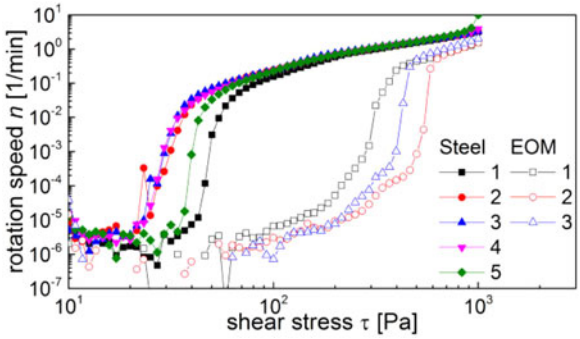

Fig. 2. Rotation speed versus shear stress for paste P4 measured with plate–plate geometry (stainless steel plate (solid points) and EOM covered plate (open points)) at a gap size of 1 mm.

poly(stearyl methacrylate) (PSMA, $M_w = 41$ kg/mol) in the highly isoparaffinic hydrocarbon Nexbase 3030 (Neste Corporation), Thixatrol ST (Elementis Specialties) as thixotrope, DISPERBYK-111 (BYK-Chemie GMBH) as dispersant, and trimethyl hydroxypentyl isobutyrate (Texanol, Eastman Chemical Company) and triacetin (Sigma-Aldrich Corporation) as solvents. The fraction of Texanol and triacetin was varied in V1–V4, whereas Polymer solution, thixotrope, and dispersant were identical. After mixing the silver powder into the vehicle, the mixture was milled with a three roll mill (Exakt 80E) to get a homogeneous paste.

Glass frit forms electric contact between the electrodes and the wafers during firing [15]–[17]. We did not include glass frites in our model formulations. These particles are typically similar in size as the silver particles used here, but the volume fraction ratio between silver and glass frit is about 20:1. Thus, it is assumed that they do not contribute to the rheological properties of the paste significantly.

III. Rheological Characterization

A. Viscosity of Vehicles

Vehicle viscosity was measured with a rotational rheometer (Anton Paar MCR 302) under shear stress control using plate–plate geometry (gap size 50 μm, diameter 25 mm) at 25 °C. Shear stress was increased stepwise and exponentially from 100 to 1000 Pa with 30 measuring points. A lapse time of 30 s per point was chosen to get a stable signal. Within experimental uncertainty, all vehicles show the same viscosity $\eta = 0.13$ Pa·s in the high shear stress range $\tau > 350$ Pa, which is used to calculate the slip layer thickness in Section IV-B.

B. Yield Stress of Silver Pastes

Yield stress was measured at 25 °C with a rotational rheometer (Haake RS150) using a four-bladed vane (diameter 10 mm) in a cup (diameter 20 mm) to avoid wall slip [18]. Shear stress was increased exponentially from 10 to 1000 Pa stepwise and exponentially with 40 points. A lapse time of 30 s per point was chosen to get a stable signal. The yield stress is determined using the tangent intersection method (see Fig. 1). P1–P3 show similar values (∼450 Pa), whereas P4 exhibits a significantly higher value (∼600 Pa).

IV. Slip Velocities of Silver Pastes

A. Experimental Procedure

Slip velocity measurements were conducted with a rotational rheometer (Anton Paar MCR 302) in a controlled shear stress mode using plate–plate geometry (diameter 25 mm) at 25 °C. The shear stress increased stepwise and exponentially from 10 to 1000 Pa with 30 points in each decade. A waiting time of 30 s per point was set to get a stable signal.

Fig. 2 shows rotation speed n versus shear stress τ for sample P4 at a gap size of 1000 μm using a stainless steel plate and an EOM covered plate. After each measurement, the sample was replaced by a fresh one. Using the stainless steel plate, the rotation speed n increased by several orders of magnitude between 20 and 100 Pa and then almost linearly between 100 and 800 Pa. For $\tau > 800$ Pa, n increased dramatically due to spillage. The onset of the initial steep increase in rotation speed n is poorly reproducible with substantial scatter between different measurements, which may be related to inhomogeneity of the interface between sample and plate and depend on sample filling into the gap. However, this aspect is out of the scope of this study. Afterward, n increases linearly in a reproducible manner.

For better understanding, video snapshots of the sheared sample P4 are shown in Fig. 3 referring to test 1. After loading, the paste and the upper plate were marked with a red line. No movement of the upper plate was visible below 50 Pa. The strong increase of the rotation speed set at a critical slip stress $\tau_s \approx 50$ Pa. Above this value, the upper plate was moving. However, the 1000-μm-thick paste layer was essentially not deformed. Between 50 and 600 Pa, only a thin paste layer adjacent to the smooth upper plate was sheared. Similar observations have been reported earlier for microgel pastes [19], [20]. Between 600 and 800 Pa, a second thin layer was sheared next to the lower plate but with much lower speed than at the upper interface. For $\tau > 800$ Pa, the sample was ejected from the gap.

Hence, the following discussion will be restricted to the shear stress range between 200 and 600 Pa, in which only a thin

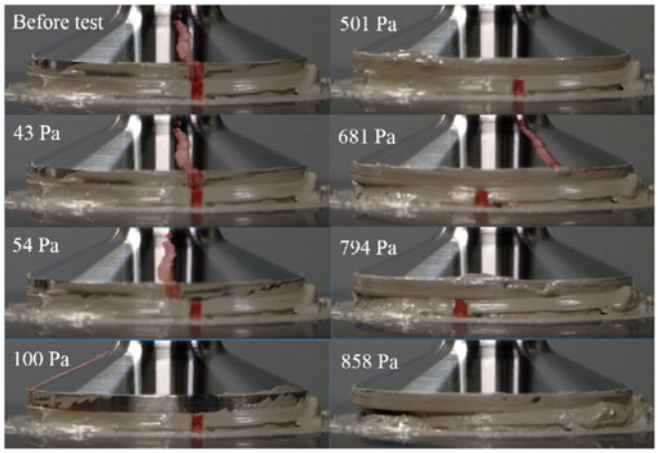

Fig. 3. Video snapshots of silver paste P4 in the gap during the measurement with plate–plate geometry and a gap size of 1 mm.

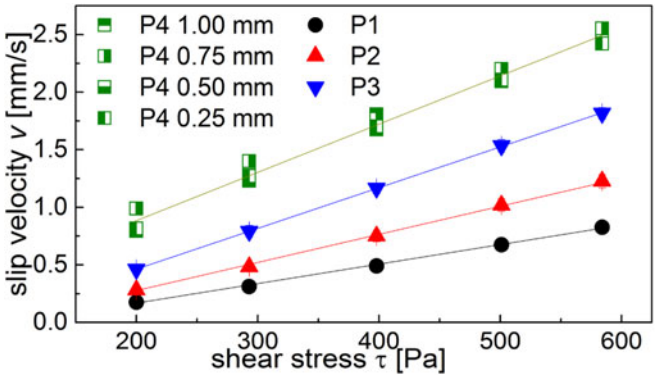

Fig. 4. Slip velocities for P4 with plate–plate geometry at different gap sizes and average slip velocities for P1–P3 calculated from measurements at different gap sizes between 0.25 and 1 mm. Lines are indicated to guide the eyes.

layer at the interface between the sample and the upper plate is sheared.

B. Slip Velocity

Based on the observation in Fig. 3, the slip velocity v at the rim of the plate is given by the rotation speed n and the plate radius R:

$$v = 2n\pi R. \tag{1}$$

According to the video snapshots, slip dominates the deformation between 200 and 600 Pa, before paste spillage. Slip velocity data are shown in Fig. 4. For all pastes, the slip velocity increases linearly with shear stress. However, as demonstrated exemplarily for sample P4, the slip velocity is independent of the gap in the investigated range between 0.25 and 1.00 mm. At a given stress, the slip velocity increases from P1 to P4 by about a factor of 4, apparently due to the variation in solvent composition.

Wall slip in suspensions is related to solid migration [21]–[23]. The thickness of the corresponding slip layer δ_{slip} depleted

TABLE II
CRITICAL STRESS FOR ONSET OF SLIP ON STEEL AND EOM COVERED PLATES

τ_s (Pa)	P1	P2	P3	P4
Steel	26 ± 5	22 ± 1	30 ± 7	41 ± 20
EOM	227 ± 26	244 ± 11	258 ± 31	369 ± 29

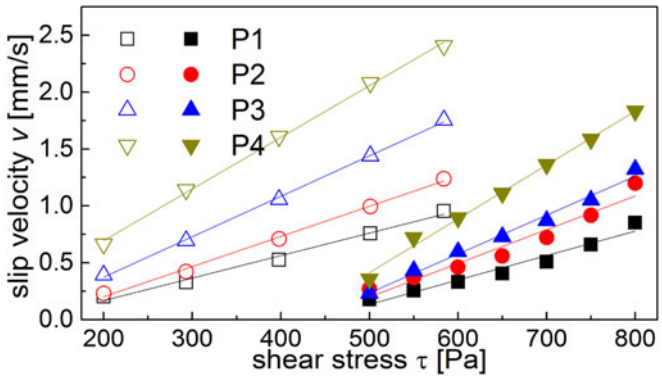

Fig. 5. Slip velocities for all four pastes measured with stainless steel plate (open points) and EOM-covered plate (solid point) at a gap size of 0.05 mm. The lines are to guide the eyes.

by particles can be calculated as

$$\delta_{slip} = \eta_s \cdot v(\tau)/\tau \tag{2}$$

where η_s is the viscosity of solvent (here, the viscosity of the vehicle should be used), $v(\tau)$ is the slip velocity, and τ is the applied shear stress [6]. Due to the linear relation between $v(\tau)$ and τ and similar viscosity η_s for the used vehicles, the slip layer thickness increases by a factor of 4 from P1–P4. Typical values are between 0.1 and 1 μm.

C. Effect of Chemical Composition of the Rheometer Plate on Wall Slip

The paste is in contact with the steel mesh as well as the polymer emulsion film (EOM) in the printing process. Slip measurements were performed with an EOM-covered plate in order to mimic this process. The EOM film was attached to the rheometer plate using a double-sided adhesive tape. The EOM roughness is about 0.5 μm, which is much smaller than the selected gap size. We did zero position calibration before each measurement. Thus, the systematic error inferred from the EOM attachment is similar for all measurements. Finally, the slip velocity is independent of gap size, as shown in Fig. 4. Hence, the uncertainty brought about by the EOM attachment seems to be negligible.

Rotation speed data exemplarily shown for sample P4 in Fig. 2 demonstrate that the critical stress for the onset of slip τ_s shifts to higher values by about one order of magnitude. Similar results have been observed for the other three pastes, as shown in Table II.

The screen opening for front-side silver paste is less than 50 μm recently. Hence, slip velocities were measured at 50-μm gap size, as shown in Fig. 5. The results agrees with those shown in Fig. 4, confirming that the slip occurs irrespective

TABLE III
PRINTING AND SCREEN PARAMETERS

Printing speed	Flooding speed	Snap-off	Pressure	
280 mm/s	400 mm/s	1.6 mm	75 N	
Line opening	Thread diameter	Fabric thickness	Emulsion thickness	Angle
35 μm	16 μm	22 μm	17 μm	30°
Tension	Mesh count	No. of fingers	No. of busbars	Busbar width
$26 + / - 2N \cdot m^{-1}$	360	102	3	1.4 mm

TABLE IV
SILVER DEPOSITS ON MONO AND POLY-SI WAFERS

	P1	P2	P3	P4
Deposit on Mono-Si (mg)	104	108	116	131
Deposit on Poly-Si (mg)	102	109	115	134
Density (g·cm^3)	5.11	5.08	5.10	5.09

of gap size. With the EOM-covered plate, the slip velocity is substantially reduced but again increases linearly with τ. This reduction is not related to the roughness of the surfaces, which is about 0.5 μm in both cases. Therefore, we attribute the observed difference to the different wetting behavior similar as discussed in [26]. Both Texanol and triacetin wet the steel surface almost completely (contact angel $\theta < 5°$), whereas the contact angle on EOM surface is $\theta \approx 15°$. For a given paste, the slop v/τ keeps the same in contact with EOM as well as steel. At a given stress τ, the slip velocity increases from P1 to P4, similar as found in contact with the steel plate. Obviously, the variation of the solvent mixture determines the formation of the slip layer depleted from particles.

V. PRINTING OF SILVER PASTES

A. Printing Process

All pastes were printed using an EKRA printer (ASYS Group, Dornstadt, Germany) equipped with a commercial screen (Brave Inc., Taiwan). Technical specifications are given in Table III.

Each paste was continuously printed with 13 polycrystalline silicon (poly-Si) wafers to reach stable conditions on the screen. The 14th poly-Si wafer was weighed before and after printing to get the deposit on the wafer. The 15th poly-Si wafer was dried after printing for geometry characterization. The 16th and 17th wafers were monocrystalline silicon (mono-Si) wafers. The next mono-Si wafer (18th) was also weighed to get the deposit. The last mono-Si wafer (19th) was dried after printing for geometry characterization. The number of finger interruptions was inspected visually for the last wafer.

The drying furnace was a D-100 (TP Solar, Inc., Downey Ave, USA), with a length of 279.4 cm, moving speed of 190.5 cm/min and setting peak temperature at 365 °C. The local temperature on the wafer surface was 245 °C. The screens were examined after printing to compare the amount of adhering pastes, using a 3-D microscope VHX-600 (Keyence Corp., Neu-Isenburg, Germany). The connections between busbar and electrodes were investigated on both mono and poly-Si wafers after drying.

B. Silver Deposit and Finger Interruption

As shown in Table IV, the silver deposit on poly- and mono-Si wafers increases by about 30% from P1 to P4. The density of the wet pastes is similar as shown in Table IV. Therefore, the measured difference in mass deposit corresponded to similar difference in volume deposit. Apparently, higher slip velocity promotes higher deposit. This is supposed to result from a corresponding reduced adhesion between paste and screen. Similar results have been obtained for solder pastes [13], [14].

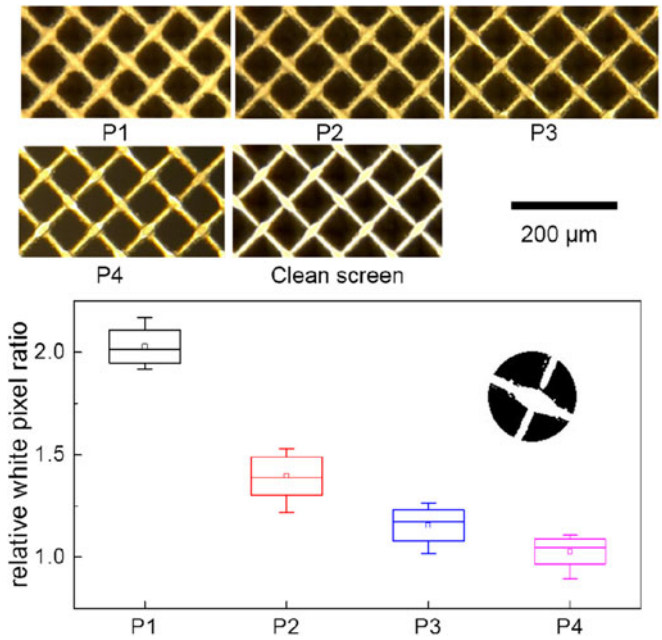

Fig. 6. Screen after printing with P1–P4 (upper) and relative white pixel ratios analysis (bottom). The inserted picture illustrates the conversion of a microscopic picture of a wire crossover into a binary picture for pixel counting.

For P1 and P2, there was no interrupted line on the last wafer according to visual inspection. For P3, there was one interrupted line, and for P4, we found three.

C. Optical Image of Screens After Printing

The deposit data discussed above are confirmed by visual inspection of the screen after printing. Images shown in Fig. 6 qualitatively reveal that the amount of paste sticking to the screen decreases from P1 to P4, and there is almost no paste sticking after printing with paste P4. Ekere *et al.* found similar differences among solder pastes during stencil printing [13], [14]. For quantitative analysis, the color pictures were transferred to binary data using the commercial software ImageJ [27], [28]. The white areas shown in the insert of Fig. 6 correspond to the steel wires with the adhering paste, 20 pictures like the circle in Fig. 6 were chosen from the binary pictures, and the white pixels in the circle were counted. Relative white pixel ratio compared with clean screen indicates that paste adhering on screen dramatically reduces from P1 to P4. We attribute the increasing silver deposit and corresponding decrease of the paste residual on the screen to the increasing slip velocity.

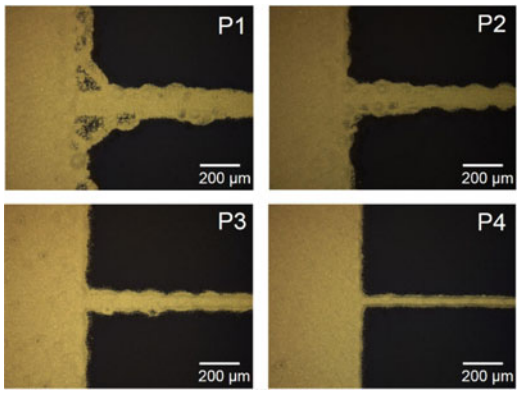

Fig. 7. Connections between fingers and busbar on monocrystalline wafers for P1–P4. The print direction is from left to right.

D. Optical Image of Connections Between Fingers and Busbar

The orientation of the busbars is perpendicular to the printing direction. The quality of connections between the fingers and busbar affects the cell efficiency. Fig. 7 illustrates the connection quality between fine electrodes and busbars on mono-Si wafers. The same trend is observed for poly-Si wafers. Quality and shape accuracy improve from P1 to P4 and seem to relate to the adhering paste on the screen. The reduced smeared area facilitates sunlight reception and should result in an increased short-circuit current j_{SC}.

VI. Optical Analysis of Printed Electrodes

A. Geometry and Shape of Silver Electrodes

The arithmetical mean roughness of mono- and poly-Si wafers is 0.656 and 0.595 μm, respectively, determined by atomic force microscopy. Systematic research has shown that the electrodes are wider on substrates with higher roughness under the same printing conditions [24], [25]. Hence, the electrodes are wider on mono- than on poly-Si wafers. Therefore, only electrodes on mono-Si wafers were analyzed using a 3-D microscope (Wyko NT 9300, Veeco Instruments Inc.).

B. Geometry Data

Several parameters of printed electrode geometry are compared for the four pastes, including shaded electrode width w_S, conductive electrode width w_C, electrode height h_f, electrode cross section A_f, and aspect ratio *AR*, defined as described in [25]. A typical electrode cross section is shown in Fig. 8(a).

Electrode geometry at 12 different positions, as indicated in Fig. 8(b), were measured. Six pictures per position of adjacent electrode sections with an area of 260 μm $\times$ 331 μm were taken. For each picture, the 3-D information of a height profile [see Fig. 9(a)] and the 2-D information of reflected light [see Fig. 9(b)] were recorded, with a resolution 0.48 μm on the *x*- and *y*-scale. A noncommercial software coded for our purposes generates the statistical data for w_S, w_C, h_f, A_f, and *AR* using all 72 recorded pictures of height profile and reflected light, respectively.

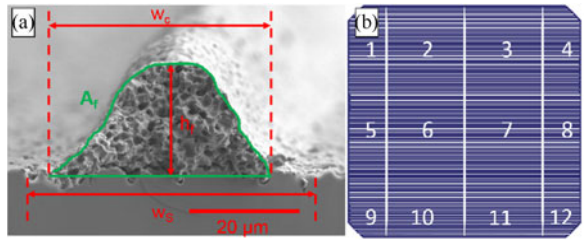

Fig. 8. (a) Description of parameters of printed electrode geometry. (b) Position of the recorded electrode geometry on the wafer surface.

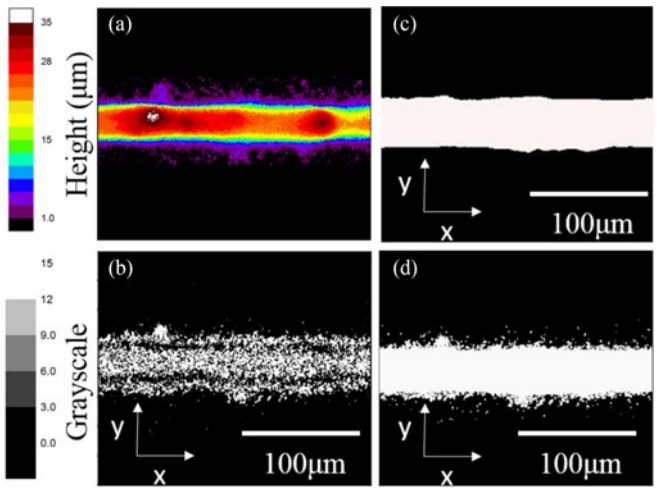

Fig. 9. (a) Original height profile data, (b) original data of reflected light in grayscale, (c) height data filtered by software for calculation of conductive linewidth $\boldsymbol{w}_c$, and (d) grayscale data filtered for calculation of shaded linewidth $\boldsymbol{w}_s$ of one line section of a wafer printed with paste P4.

The conductive electrode width w_C represents the part of printed electrode with higher height than the surface roughness of the substrate. This part of the electrode contributes to the electrical conductivity. The shaded electrode width w_S represents the area covered by the electrodes. The analysis software converts the original data into binary data as illustrated in Fig. 9 for calculation.

The electrode height h_f is detected from the height scan mode pictures by selecting the highest point for each cross section. The cross section A_f is also calculated based on the height scan mode pictures by integrating the area between the base line and the height profile as indicated in Fig. 8(a). *AR* is calculated as h_f/w_C using their average values.

The parameters w_S and w_C are depicted in Fig. 10. P4 shows narrowest w_S and w_C, whereas these values are very similar for the other three pastes. This indicates that electrode width is tightly related to the yield stress of the corresponding paste, since the yield stress of paste P4 is significantly higher than that of the other three pastes.

The values for the parameters h_f, A_f, and *AR* of the investigated electrodes are shown in Fig. 11. h_f and A_f increase with slip velocity (from P1 to P4), mainly due to higher deposits. Higher h_f and A_f should enable lower series resistance when printing with narrower screen opening. Finally, high h_f and low

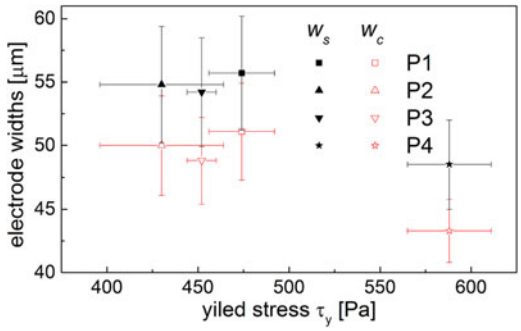

Fig. 10. Relation between electrodes widths (w_s and w_c) and yield stress.

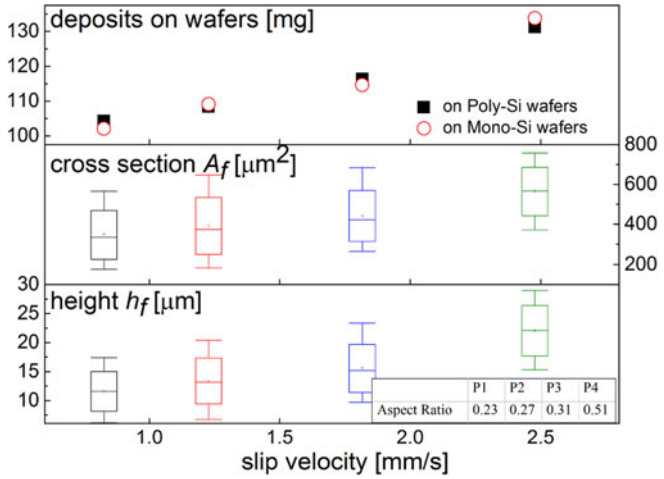

Fig. 11. Deposit, electrode cross section, height, and aspect ratio versus characteristic slip velocity. The slip velocity was measured with steel plate at shear stress of 598 Pa. Corresponding data are shown in Fig. 4.

w_c result in a higher ratio *AR*, and accordingly, this parameter increases substantially from P1 to P4.

In a previous study, w_s, w_c, and h_f were gained at (47, 65, 7 μm) and (22, 47, 12 μm) printed with 30-μm screen and stencil, respectively [29]. The results in this study reached a similar level.

In summary, the characterization of the screen-printed electrode geometry revealed significant differences with respect to electrode widths w_S and w_C, height h_f, cross-sectional area A_f, and aspect ratio *AR*. These parameters are directly related to the pastes' yield stress (w_s, w_c, and *AR*) and particularly to the adhesion or slip in contact with the screen (h_f, A_f, and *AR*) controlling the paste deposit.

C. Theoretical Calculation of the Relative Impact of the Parameters

The short-circuit current j_{sc} and the fill factor *FF* are influenced by the shaded area and grid resistances. The influence of these two parameters can be estimated based on the corresponding values for the shaded electrode width and cross section with the equations mentioned in [25]. The properties of the busbars (width, height, and specific resistance) are assumed equal for all pastes.

The metallized fraction on the wafer, $A_{met,grid}$, can be calculated using the shaded electrode width w_s along the finger direction. Total current density loss due to the grid, $\Delta j_{sc,grid}$, is calculated assuming the photon-generated current is 40 mA/ cm^2. Assuming a specific line resistance $\rho = 2.5\,\mu\Omega\cdot$ cm, the line resistance $R_L = \rho/A_f$ is calculated, using original cross-sectional data varying along the line direction. Series resistance $\Delta r_{s,grid}$ and fill factor loss ΔFF_{grid} are also calculated correspondingly. All the data are summarized in Table V.

In conclusion, the calculated $\Delta j_{sc,grid}$ is lower for a wafer metallized with paste P4 than for a wafer with paste P1–P3, and this is attributed to P4's higher yield stress. The calculated loss in fill factor ΔFF_{grid} decreases monotonically from P1 to P4, i.e., with increasing slip velocity of the pastes. The less loss of these two parameters indicates a higher efficiency when printed with P4.

TABLE V
THEORETICAL CALCULATION OF THE RELATIVE IMPACT DUE TO THE GEOMETRICAL PARAMETERS

	P1	P2	P3	P4
w_s [μm]	55.74	54.81	54.24	48.48
A_f [μm^2]	347.86	393.83	441.51	564.94
h_f [μm]	11.59	13.41	15.55	22.03
AR	0.23	0.27	0.31	0.51
$A_{met,grid}$ [%]	5.59	5.53	5.49	5.11
$\Delta j_{sc,grid}$ [mA/cm^2]	2.24	2.21	2.20	2.05
R_L [Ω/m]	81.82	72.95	61.95	47.04
$\Delta r_{s,grid}$ [$\Omega\cdot$cm^2]	0.27	0.24	0.20	0.15
ΔFF_{grid} [%abs]	1.52	1.36	1.15	0.88

VII. CONCLUSION

Four silver pastes with different organic vehicles have been investigated regarding their yield stress as well as their adhesion or slip behavior in contact with stainless steel and EOM surfaces.

The critical stress for the onset of slip τ_s and the slip velocity v have been determined using a rotational rheometer equipped with a plate–plate geometry. Slip velocity is independent of the chosen gap size but increases linearly with applied stress. The onset of slip on EOM surface occurs at about an order of magnitude higher stresses, and at a given stress, slip velocity is substantially lower compared with the steel surface, since the pastes wet steel better than EOM. However, there is a strong influence of vehicle on the slip phenomenon, and the absolute value of v_s and the slope v_s/τ increase strongly from paste P1 to P4. Obviously, different solvent mixtures result in the formation of different slip layers. However, the yield stress is similar for pastes P1–P3 ($\tau_y \approx 450$ Pa), whereas P4 a significantly higher value ($\tau_y = 588$ Pa).

The pastes have been printed on mono- and poly-Si wafers. The silver deposit, the residual on the screen, and the busbar/finger connection have been determined using gravimetric and optical methods. The geometry of the printed electrodes has been analyzed using optical microscopy and image analysis.

The silver deposit on both types of wafers increased, and correspondingly, the residual silver on the screen decreased from paste P1 to P4, i.e., with increasing slip velocity. The area of the junction between busbar and finger electrode also strongly decreases with increasing slip. Shaded and conductive electrode widths are similar for pastes P1–P3 within experimental accuracy, but corresponding values for P4 are significantly lower, and this is attributed to its higher yield stress. Electrode cross section and height monotonically increase from P1 to P4, i.e., with increasing slip velocity. Finally, the aspect ratio $AR = h_f/w_c$ increases from P1 to P4, and the value for paste P4 is especially high, $AR(\mathrm{P4}) = 0.5$. This seems to be a combined effect of high yield stress and high slip velocity.

Silver deposit, shape of the busbar/finger junction, and electrode geometry are known to have an important impact on electrical cell parameters. Theoretical calculation indicates an increase of short-circuit current and fill factor from P1 to P4 due to the change in geometrical parameters. Hence, overall cell efficiency may be controlled by the slip behavior of the wet paste in contact with the printing screen.

ACKNOWLEDGMENT

The authors would like to acknowledge fruitful discussions about image analysis with Dr. H. Dietsch (BASF SE). Technical support by M. Czink and M. Machate (both from BASF SE), as well as 3-D microscopy measurements provided by BASF analytics, are also gratefully acknowledged.

REFERENCES

[1] S. B. Rane *et al.*, "Firing and processing effects on microstructure of fritted silver thick film electrode materials for solar cells," *Mater. Chem. Phys.*, vol. 82, no. 1, pp. 237–245, 2003.

[2] K. K. Hong *et al.*, "Mechanism for the formation of Ag crystallites in the Ag thick-film contacts of crystalline Si solar cells," *Sol. Energy Mater. Sol. Cells*, vol. 93, no. 6, pp. 898–904, 2009.

[3] R. Faddoul, N. Reverdy-Bruas, and J. Bourel, "Silver content effect on rheological and electrical properties of silver pastes," *J. Mater. Sci: Mater. Electron.*, vol. 23, no. 7, pp. 1415–1426, 2012.

[4] M. Pospischil *et al.*, "Paste rheology correlating with dispensed finger geometry," *IEEE J. Photovoltaics*, vol. 4, no. 1, pp. 498–503, Jan. 2014.

[5] S. Thiberta *et al.*, "Influence of silver paste rheology and screen parameters on the front side metallization of silicon solar cell," *Mater. Sci. Semicond. Process.*, vol. 27, pp. 790–799, 2014.

[6] F. Soltani and U. Yilmazer, "Slip velocity and slip layer thickness in flow of concentrated suspensions," *J. Appl. Polymer Sci.*, vol. 70, no. 3, pp. 515–522, 1998.

[7] U. Yilmazer and D. M. Kalyon, "Slip effects in capillary and parallel disk torsional flows of highly filled suspensions," *J. Rheol.*, vol. 33, no. 8, pp. 1197–1212, 1989.

[8] H. A. Barnes, "A review of the slip (wall depletion) of polymer solutions, emulsions and particle suspensions in viscometer: its causes, character, and cure," *J. Non-Newton. Fluid*, vol. 56, no. 3, pp. 221–251, 1995.

[9] D. M. Kalyon, "Apparent slip and viscoplasticity of concentrated suspensions," *J. Rheol.*, vol. 49, no. 3, pp. 621–640, 2005.

[10] A. Yoshimura and A. K. Prud'homme, "Wall slip corrections for Couette and parallel disk viscometers," *J. Rheol.*, vol. 32, no. 1, pp. 53–67, 1988.

[11] R. Buscall, J. I. McGowan, and A. J. Morton-Jones, "The rheology of concentrated dispersions of weakly attracting colloidal particles with and without wall slip," *J. Rheol.*, vol. 37, no. 4, pp. 621–641, 1993.

[12] B. K. Aral and M. K. Dilhan, "Effects of temperature and surface roughness on time-dependent development of wall slip in steady torsional flow of concentrated suspensions," *J. Rheol*, vol. 38, no. 4, pp. 957–972, 1994.

[13] R. Durairaj, S. Mallik, A. Seman, and N. N. Ekere, "Investigation of wall-slip effect on lead-free solder paste and isotropic conductive adhesives," *Sadhana*, vol. 34, no. 5, pp. 799–810, 2009.

[14] R. Durairaj, L. W. Man, N. N. Ekere, and S. Mallik, "The effect of wall-slip formation on the rheological behaviour of lead-free solder pastes," *Mater. Des.*, vol. 31, no. 3, pp. 1056–1062, 2010.

[15] C. Ballif, D. M. Huljic, G. Willeke, and A. Hessler-Wyser, "Silver thick-film contacts on highly doped n-type silicon emitters: Structural and electronic properties of the interface," *Appl. Phys. Lett.*, vol. 82, no. 12, pp. 1878–1880, 2003.

[16] G. Schubert, F. Huster, and P. Fath, "Physical understanding of printed thick-film front contacts of crystalline Si solar cells—Review of existing models and recent developments," *Sol. Energy Mater. Sol. Cells*, vol. 90, no. 18, pp. 3399–3406, 2006.

[17] J. Fields *et al.*, "The formation mechanism for printed silver-contacts for silicon solar cells," *Nature Commun.*, vol. 7, 2016, Art. no. 11143.

[18] H. A. Barnes and J. O. Carnali, "The vane-in-cup as a novel rheometer geometry for shear thinning and thixotropic materials," *J. Rheol.*, vol. 34, no. 6, pp. 841–866, 1990.

[19] S. P. Meeker, R. T. Bonnecaze, and M. Cloitre, "Slip and flow in soft particle pastes," *Phys. Rev. Lett.*, vol. 92, no. 19, 2004, Art. no. 198302.

[20] S. P. Meeker, R. T. Bonnecaze, and M. Cloitre, "Slip and flow in pastes of soft particles: Direct observation and rheology," *J. Rheol.*, vol. 48, no. 6, pp. 1295–1320, 2004.

[21] G. Segre and A. Silberberg, "Radial particle displacements in poiseuille flow of suspensions," *Nature*, vol. 189, no. 4760, pp. 209–210, 1961.

[22] G. Segre and A. Silberberg, "Behaviour of macroscopic rigid spheres in Poiseuille flow Part 1. Determination of local concentration by statistical analysis of particle passages through crossed light beams," *J. Fluid Mech.*, vol. 14, no. 01, pp. 115–135, 1962.

[23] V. Seshadri and S. P. Sutera, "Apparent viscosity of coarse, concentrated suspensions in tube flow," *Trans. Soc. Rheol.*, vol. 14, no. 3, pp. 351–373, 1970.

[24] M. Aoki *et al.*, "30 μm fine-line printing for solar cells," in *Proc. IEEE 39th Photovoltaic Spec. Conf.*, 2013, pp. 2162–2166.

[25] A. Lorenz *et al.*, "Impact of texture roughness on the front-side metallization of stencil-printed silicon solar cells," *IEEE J. Photovoltaics*, vol. 5, no. 4, pp. 1237–1244, Jul. 2015.

[26] J. R. Seth, M. Cloitre, and R. T. Bonnecaze, "Influence of short-range forces on wall-slip in microgel pastes," *J. Rheol.*, vol. 52, no. 5, pp. 1241–1268, 2008.

[27] C. A. Schneider, W. S. Rasband, and K. W. Eliceiri, "NIH Image to ImageJ: 25 years of image analysis," *Nature Methods*, vol. 9, no. 7, pp. 671–675, 2012.

[28] J. Schindelin *et al.*, "Fiji: An open-source platform for biological-image analysis," *Nature Methods*, vol. 9, no. 7, pp. 676–682, 2012.

[29] V. Shanmugam *et al.*, "Analysis of fine-line screen and stencil-printed metal contacts for silicon wafer solar cells," *IEEE J. Photovoltaics*, vol. 5, no. 2, pp. 525–533, Mar. 2015.

Authors' photographs and biographies not available at the time of publication.